Experimental and Numerical Investigation of the Turbulent Boundary Layer of a Grazing Flow Over Porous Materials

Moriaux, O.K.M.; Zamponi, R.; Satcunanathan, Sutharsan ; Matthias, Meinke; Schröder, Wolfgang

DOI
10.2514/6.2024-3050

Publication date
2024

Document Version
Final published version

Published in
30th AIAA/CEAS Aeroacoustics Conference (2024)

Citation (APA)
Moriaux, O. K. M., Zamponi, R., Satcunanathan, S., Matthias, M., & Schröder, W. (2024). Experimental and Numerical Investigation of the Turbulent Boundary Layer of a Grazing Flow Over Porous Materials. In *30th AIAA/CEAS Aeroacoustics Conference (2024)* Article AIAA 2024-3050 (30th AIAA/CEAS Aeroacoustics Conference, 2024). https://doi.org/10.2514/6.2024-3050

Aeroacoustics Conferences
June 4-7, 2024, Rome, Italy
30th AIAA/CEAS Aeroacoustics Conference (2024)

10.2514/6.2024-3050

Experimental and Numerical Investigation of the Turbulent Boundary Layer of a Grazing Flow Over Porous Materials

Olivier Moriaux*
Delft University of Technology, 2629HS Delft, South Holland, The Netherlands

Riccardo Zamponi†
von Karman Institute for Fluid Dynamics, 1640 Sint-Genesius-Rode, Flemish Brabant, Belgium
Delft University of Technology, 2629HS Delft, South Holland, The Netherlands

Sutharsan Satcunanathan‡, Matthias Meinke§, and Wolfgang Schröder¶
RWTH Aachen University, Aachen 52062, Germany

The aeroacoustic performance of porous materials for sound-control applications depends on the flow communication through the medium. Hence, flow-permeable noise-reduction technologies should be tailored to the flow they operate within. A large-scale simulation setup has been developed in this work to aid the design of porous materials for airframe-noise mitigation by modeling their aerodynamic and acoustic behavior. However, this aerodynamic modeling setup requires validation on a more fundamental flow case. To this purpose, large-eddy simulations of the turbulent boundary-layer flow over two porous materials and a reference solid wall are compared against wind-tunnel measurements. This analysis includes velocity-derived boundary-layer profiles and unsteady wall-pressure measurements on the upper and lower surfaces of the flow-permeable medium. The generated experimental data are additionally made publicly available as a benchmark for boundary-layer flows over a porous wall-insert. The results of the simulation show a satisfactory agreement with the experimental data in most cases, especially for the solid wall. The mean-velocity and turbulence-intensity profiles and the wall-pressure spectra of the boundary layer over the porous materials show a dependence on the streamwise position along the surface, leading to a decrease in wall-pressure energy below a Strouhal number based on the boundary-layer thickness and the outer-flow velocity of 3 and an increase above it. Future research will be aimed at developing a new model for porous media flow centered on the optimization of the flow communication paths within them. This will potentially allow the development of porous materials with favorable acoustic properties while minimizing their aerodynamic penalty.

I. Introduction

TURBULENT flow interaction with landing gear and high-lift devices during the take-off and landing phases of flight constitutes a significant noise source [1]. With the continued growth in air traffic and the many negative impacts of noise on people [2], the reduction of such airframe noise forms a crucial field of research [1, 3].

Several passive noise-mitigation technologies, such as vortex generators, serrations, and porous materials, are being investigated. Among these options, porous materials have shown considerable promise in reducing such noise sources [1]. Multiple mechanisms have been shown to contribute to sound mitigation, many of which are actively being studied. For instance, with the reduced resistivity of the porous material to velocity fluctuations at the surface, the magnitude of the hydrodynamic wall-pressure fluctuations, which are the source of some major noise-generation mechanisms [4, 5], can be reduced [6]. With leading-edge porous treatments, incoming turbulence distortion is altered, resulting in a noise abatement around the vortex-shedding tone. However, this decreased flow resistivity also increases the surface roughness, leading to increased high-frequency noise and drag [7]. Rubio Carpio et al. [8] show that for porous trailing

---

[*] Ph.D student, Flow Physics and Technology, o.k.m.moriaux@tudelft.nl, AIAA Student Member.

[†] Research Professor, Environmental and Applied Fluid Dynamics, riccardo.zamponi@vki.ac.be, AIAA Member.

[‡] Research Scientist, Institute of Aerodynamics, s.satcunanathan@aia.rwth-aachen.de.

[§] Senior Scientist, Institute of Aerodynamics, m.meinke@aia.rwth-aachen.de.

[¶] Professor, Institute of Aerodynamics, office@aia.rwth-aachen.de, AIAA Member.

edges, flow communication across the material is crucial to achieving noise abatement. Similarly, the improvement in drag with porous treatment is only observed by Ali et al. [9] when the boundary layer can penetrate into the inner volume.

Yet, the penetration of the flow into or through the porous material carries several disadvantages too. The flow recirculation within the medium might result in additional noise over a small range of frequencies [9]. Due to the balancing of the steady pressure difference between both sides of the airfoil, drag is increased while lift is decreased [8]. Furthermore, additional noise sources are associated with the transpiration velocity of flow through the porous surface [6, 10]. The streamwise distribution of all these noise sources can result in interference between them [11].

Due to the many aspects affecting the aerodynamic and acoustic performance of porous materials, they need to be designed for each specific use case. A combination of computational fluid dynamics (CFD) and computational aeroacoustics (CAA) allows for such case-dependent optimization of the porous-material design and implementation. A simulation of the full skeleton of a flow-permeable medium is too restrictive in most cases due to the computational cost of having to resolve these minute scales. Hence, for the CFD aspect, a large-eddy simulation (LES) using a homogeneous medium representation of the material is considered [6]. Such a method should still be able to capture many of the aforementioned aerodynamic and acoustic aspects while considering the large-scale geometry within which the porous medium is implemented. To develop such an approach for turbulent boundary layers over a porous surface, empirical data on flow over and through a permeable medium is needed to calibrate and validate the models.

Consequently, the aim of the present research is twofold: (i) the acquisition of a benchmark dataset of a turbulent boundary layer flow over a porous material, which is made publicly available [12], and (ii) the validation of a numerical model for a porous material in CFD simulations. The generation of this dataset can additionally serve as a test bench for the development of a new modeling approach for flow through porous media. To this purpose, a reference solid wall insert and two porous inserts are installed within an acoustically treated wind tunnel. The boundary-layer profiles over the inserts are measured with a hot-wire anemometer (HWA), whereas the wall-pressure fluctuations on the upper and lower surfaces of the porous wall inserts are acquired with remote microphone probes (RMP).

The document is structured in the following way. The modeling and specification of the porous-material samples and the setups of the experimental wind-tunnel tests and numerical simulations are outlined in Section II. The validation of the numerical data is performed in Section III, where the results are also analyzed. Section IV provides some concluding remarks and mentions the future research to be performed with the presented data.

II. Methodology

The setups of both the experimental and numerical studies are discussed in this section. A crucial element of the measurement campaign is the acquisition of wall-pressure spectra (WPS) and velocity profiles over the solid and porous wall inserts, which serve to validate the numerical simulation. The wind tunnel employed in this investigation is briefly introduced in Section II.A. The modeling approach of the porous media and the model parameters are discussed in Section II.B. The considered porous materials and their calibration for the aforementioned modeling are shown in Section II.C. The HWA setup and comparison approach with the CFD data are mentioned in Section II.D. The design of the RMPs and the processing of the WPS are explained in Section II.E. Lastly, the details regarding the CFD setup are provided in Section II.F.

A. WAABLIEF wind tunnel

The WAABLIEF wind tunnel (**W**ind tunnel for **A**ero**A**coustic **B**oundary **L**ayer **I**ncluding pr**E**ssure gradient e**F**fect) [13] is used for its strong acoustic treatment to limit background noise in the pressure measurements. The origin of the coordinate system is situated in the center of station 2 of WAABLIEF [13], at the lower wall, where all analyzed solid and porous wall-inserts are mounted (see Fig. 1a). The cross-section of the test section is $(y, z) = (h, h)$, with $h = 0.25$ m. Here, x is the streamwise coordinate axis, y is the wall-normal coordinate axis, and z is the spanwise coordinate axis. A boundary layer trip is positioned 1.4 m upstream of station 2 to force the transition from laminar to turbulent flow to happen at a known location, as indicated in Fig. 1a. This enables the simulation to more closely represent the wind-tunnel conditions. For the trip, three 1 mm strips of sandpaper are used with a 1 mm spacing between them. A detailed description of the facility is provided by Van de Wyer et al. [13]. Note that the wind-tunnel inlet and settling chamber have since been updated, further improving the acoustic performance of the wind tunnel.

B. Porous-material parameterization

To correctly model the fluid flow through the porous material, the Darcy-Forchheimer model [14] is considered, which accounts for both the pressure gradient acting upon the flow through the material and the inertia of the flow:

$$-\frac{\partial p}{\partial x} = K^{-1}\phi\mu u + K^{-1/2}\phi^2 c_{\mathrm{F}}\rho u^2. \tag{1}$$

Here, $\partial p/\partial x$ is the pressure gradient acting within a point in the porous medium in the direction of the fluid motion, K denotes the static permeability, ϕ is the porosity, μ is the dynamic viscosity of the fluid, c_{F} is the Forchheimer coefficient, ρ is the fluid density, and u is the local flow velocity.

The porosity is defined as the fraction of the flow-permeable volume within the porous medium, i.e., not the solid material skeleton nor any closed cavity unreachable by the flow, to the total volume of the porous medium. The static permeability quantifies how much resistance the porous medium presents to flow through it. The Forchheimer coefficient scales the Forchheimer correction term in Eq. (1). Hence, c_{F} indicates how strongly the flow within the material is affected by inertial effects.

A limitation of this model is that it considers the porous medium to have a homogeneous and isotropic pore structure [14]. The permeable material is modeled as a homogeneous continuum with volume-averaged properties, hence the distinct porous material skeleton is not considered. This means that no coupling between the skeleton and the flow is modeled, i.e., no elastic or thermal effects linked to the porous material [6].

C. Diamond-lattice structure

In the context of the EU-funded project INVENTOR [15], a porous material structure was designed with a diamond-lattice pattern named DMND, shown in Fig. 1b. This porous structure is scaled with the unit-cell size d_c to alter the permeability of the material while retaining the same porosity. Two porous materials are considered in this investigation with $d_c = \{3.5\,\mathrm{mm}, 4.5\,\mathrm{mm}\}$. The solid reference wall-insert is indicated with $d_c = 0\,\mathrm{mm}$. This porous material is tiled to form a wall-insert with dimensions of $(x, y, z) = (10\,\mathrm{cm},\ 2.5\,\mathrm{cm}, 10\,\mathrm{cm})$, as shown in Figs. 1a and 1c. The streamwise length of the wall-insert is used as a reference length, $L = 10\,\mathrm{cm}$.

To properly model the porous materials, the parameter values for the Darcy-Forchheimer model (see Eq. (1)) are estimated using the method and experimental calibration setup described by Rubio Carpio et al. [16]. The static pressure drop Δp through porous samples of thickness t when subject to a defined flow rate is measured and matched to the Hazen-Dupuit-Darcy quadratic equation [17]:

$$\frac{\Delta p}{t} = \frac{\mu}{K} v_d + \rho C v_d^2, \tag{2}$$

where C is the form coefficient, and v_d is the Darcian velocity. The latter is defined as the volumetric flow rate per cross-sectional area of the porous material sample.

Similarly to Zamponi et al. [18, 19], the static pressure drop is determined with two ports located at a distance of 50 mm on either side of the test section containing the sample. The differential pressure is acquired by a Mensor 2101, which is stated to have an accuracy of 2 Pa. Upstream of the test pipe, an Aventics pressure regulator is used to control the flow rate, which is monitored with a TSI 4040 flow meter, which provides an accuracy of 2 % on the read value [16]. The calibration data of both materials are shown in Fig. 2, where $R = \Delta p/(t\ v_d)$ is the static air-flow resistivity.

Several sample thicknesses are tested to investigate the potential entrance or exit effects on the acquired pressure drop that may be present for thin porous samples [16]. Whereas both R and K appear unaffected by the changing thicknesses of the samples, C is strongly impacted (see Fig. 2c). The final model parameters used by the numerical simulation are listed in Table 1.

Table 1 Darcy-Forchheimer model parameters for the two DMND porous materials.

d_c, mm	ϕ, -	K, mm^2	c_{F}, -
3.5	0.617	6.032	0.8175
4.5	0.617	9.016	0.6814

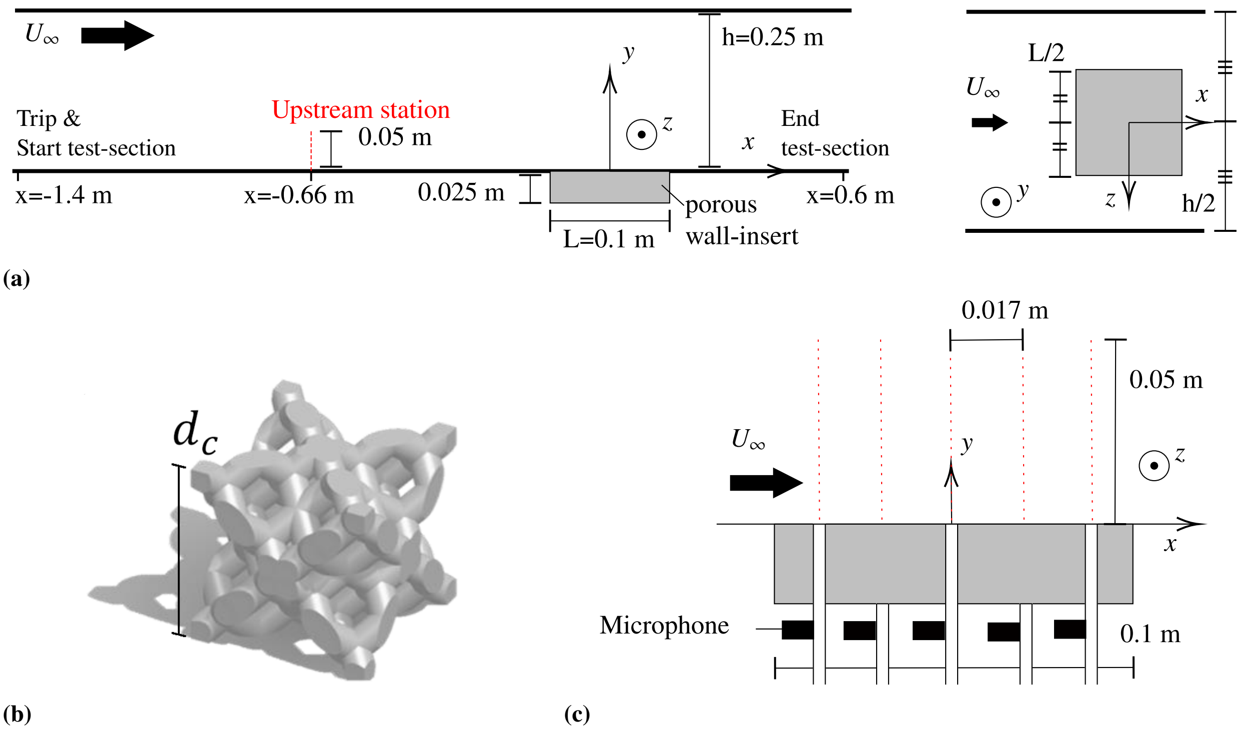

Fig. 1 Diagrams of the test section, porous material wall-insert, and the measurement locations. (a) WAABLIEF wind tunnel test section geometry projected on the xy and xz planes. (b) Porous DMND unit structure. (c) RMP and HWA traverse locations in station 2 of WAABLIEF [13]. Solid or porous wall insets are indicated by the grey rectangle. HWA traverses are indicated by the red dotted lines. Diagrams not to scale.

D. HWA setup

The boundary-layer profiles are acquired with a single-component constant-temperature Dantec HWA probe. The Dantec StreamWare software with the Dantec StreamLine Pro anemometry system ensures that all velocity fluctuations above the cut-off frequency of 10.6 kHz are filtered out. Five vertical profiles are obtained along the wall-inserts to analyze the streamwise development of the boundary layer: $x/L = \{-0.33,\ -0.17,\ 0,\ 0.17, 0.33\}$ with $z/L = 0$ (see Fig. 1c). A single upstream profile at $x/L = -6.6$ is acquired to help define the inlet conditions of the simulation (see Fig. 1a).

Each profile has a separate height calibration. A 2D (XY) robotized traverse system is used for the five main profiles, with a spatial resolution of 5×10^{-3} mm, which results in a coordinate accuracy of $\pm 2.5 \times 10^{-3}$ mm. For all the solid-wall measurement cases, the height calibration of the profiles is further tweaked a-posteriori by comparing the inner-scaled boundary-layer profile with the theory of a zero-pressure-gradient turbulent boundary-layer profile.

The order of acquisition of the five vertical profiles is randomized to not introduce measurement error-related trends to the parameter x/L. Several duplicate probe points are acquired at the end of each vertical profile to correct the measured hot-wire voltages for thermal effects using the model of Kanevče and Oka [20]. According to this correction, the measured hot-wire voltage E_w at flow temperature T_a is corrected to the voltage $E_{w,\text{ref}}$ that would be measured at a reference temperature $T_{a,\text{ref}}$, given the wire temperature T_w:

$$E_{w,\text{ref}} = E_w \left[\frac{T_w - T_{a,\text{ref}}}{T_w - T_a} \right]^{1/2}. \tag{3}$$

The wire temperature is estimated with Eq. (4) [7]. Each set of duplicate measurements, indicated with subscripts 1 and 2, provides an estimate for T_w:

$$T_w = \frac{E_{w,1}^2 T_{a,2} - E_{w,2}^2 T_{a,1}}{E_{w,1}^2 - E_{w,2}^2}. \tag{4}$$

The turbulent length scale (Λ) computation uses the assumption of frozen turbulence. Here, the time scale of the

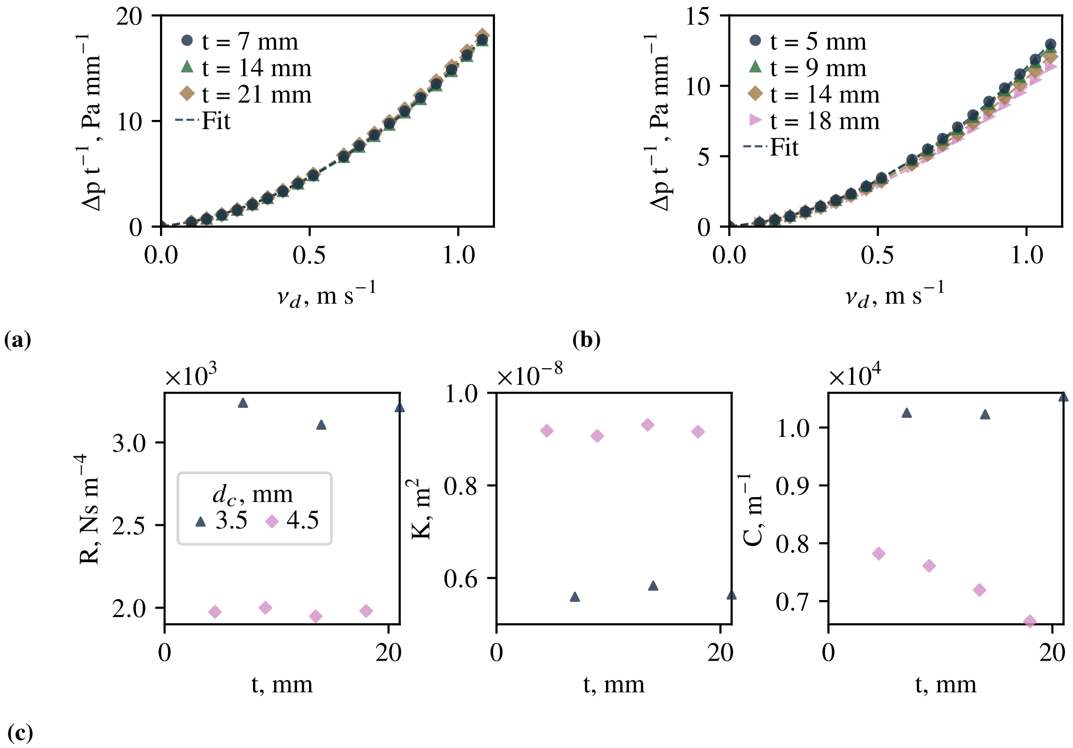

(a) **(b)**

(c)

Fig. 2 Calibration data of DMND porous-material samples. Pressure drop through porous samples with: (a) $d_c = 3.5\,\text{mm}$**, (b)** $d_c = 4.5\,\text{mm}$**. (c) Model parameters of the Hazen-Dupuit-Darcy equation [17] for both materials.**

turbulence is chosen to be the first crossing of the auto-correlation of the velocity fluctuations signal $R_{U'U'}$ with the value of e^{-2} [7]:

$$R_{U'U'}(\tau) = \lim_{T\to\infty} \int_0^T U'(t)U'(t+\tau)\mathrm{d}t. \tag{5}$$

Prior to the computation of the turbulent length scale, the velocity fluctuations are low-pass filtered with a Butterworth filter of the 5th order and a critical frequency of 0.2 Hz.

Lastly, as noted by Zamponi et al. [21], a single-component HWA is only sensitive to fluctuations of the velocity in the direction of the mean-velocity vector. Hence, the turbulence intensity (TI) reported in Section III is not simply the TI of the velocity in the streamwise direction. Therefore, the TI and Λ of the CFD in Fig. 7 consider velocity fluctuations that are defined as

$$U' = \sqrt{\left(u'_x \cos\alpha\right)^2 + \left(u'_y \sin\alpha\right)^2}; \qquad \text{with} \quad \alpha = \arctan\left(\overline{u}_y/\overline{u}_x\right). \tag{6}$$

Here, u_x and u_y are the velocities in the x and y axes, respectively, with u'_i being the velocity fluctuation with respect to the mean-flow velocity $\overline{u}_i$, and α the local mean flow direction. The mean-velocity data discussed in Section III, i.e., $\overline{u}$, represent the magnitude of the mean-velocity vector in the x and y axes.

E. RMP: Semi-infinite waveguide probe

The solid and porous wall-inserts are instrumented with 5 RMPs, which acquire unsteady wall-pressure fluctuations, as shown in Fig. 1c. Three RMPs are situated on the upper surface of the solid and porous inserts at $x/L = \{-0.33,\ 0, 0.33\}$, while two RMPs are positioned on the lower surface of the porous materials at $x/L = \{-0.17, 0.17\}$.

The RMPs are semi-infinite waveguide probes [22] (see Fig. 3a) that minimize the reflection of pressure waves within the probe, i.e., resonance. As such, the probe orifice connects to a long main tube with an anechoic termination. Attached to the side of the main tube is a side branch instrumented with a GRAS 40PH microphone, which has a flat frequency response of ±2 dB from 10×10^{-3} kHz to 20 kHz [23]. The distance between the orifice and side branch differs between the RMPs instrumenting the upper and lower porous-material surfaces, being 40 mm and 15 mm, respectively.

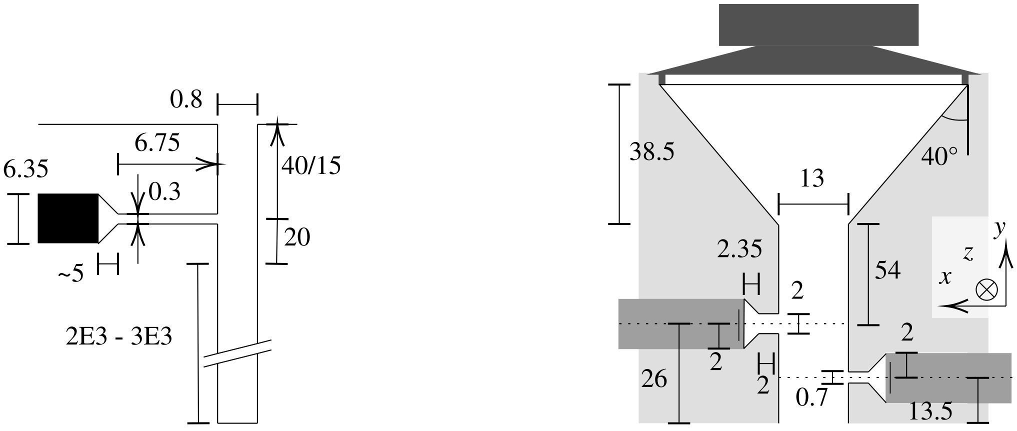

(a) **(b)**

Fig. 3 Diagrams of the RMP and calibrator. Diagrams not to scale. (a) RMP geometry in mm**. The tube section above the side branch is** 40 mm **when instrumenting the upper surface of the wall-insert and** 15 mm **when instrumenting the lower surface. Attenuation tubes vary in the region of** 2 m **to** 3 m**. A plastic capillary tube is slip-fit over a metallic one** 20 mm **below the RMP side branch. The depth dimension of the transducer cavity is a rough estimate. (b) Plane-wave tube calibrator geometry in** mm **and degrees.**

The RMPs are calibrated using the hardware setup described by Moriaux et al. [22]. The plane-wave tube calibrator has two microphone-backed side branches and a speaker on top (see Fig. 3b). The lower open end of the calibrator is first positioned over a flush-mounted reference microphone and then over the RMP. All calibrator and reference microphones are quarter-inch GRAS 40PH microphones. The transfer functions (TF) between these microphones are computed using a Python implementation [24, 25] of the MATLAB 'tfestimate' function [26]. Combining the TFs from both calibration steps yields the full TF between the reference microphone and RMP.

In order to remove calibrator-induced resonance from the RMP calibration, such that no spurious resonance is introduced into the TF-corrected WPS, the semi-empirical calibration approach developed by Moriaux et al. [22], i.e., ASSIST (B**A**yesian proce**S**sing of **S**pur**I**ous re**S**onance in calibra**T**ion data), is used. This method fits the model of Whitmore [27] for the frequency-response of branching geometries made of line-cavity elements to the calibration data with Bayesian inference. As such, all resonance that is plausible under the presumed geometry of the probe is retained while removing and replacing resonance from other sources, such as the calibrator. For a detailed guide on the use of the publicly available Python code repository [24, 25], the reader is referred to Moriaux and Zamponi [28].

The frequency axis of the WPS is normalized with the boundary layer thickness δ and the outer-flow velocity U_e, forming the Strouhal number St. The WPS is similarly rescaled to be normalized by St. The WPS are only presented at St numbers where they lie at least $3\,\mathrm{dB\,St^{-1}}$ above the background-noise measurements, which are acquired with the wind-tunnel fan turned off.

The boundary-layer profiles derived from the HWA measurements, the boundary-layer parameters, the WPS, and the WPS of the background noise are made available in a public repository [12]. The generated data are available for the three considered wall-inserts $d_c = \{0\,\mathrm{mm},\ 3.5\,\mathrm{mm}, 4.5\,\mathrm{mm}\}$, at three inflow velocities $U_e = \{15\,\mathrm{m\,s^{-1}},\ 20\,\mathrm{m\,s^{-1}}, 25\,\mathrm{m\,s^{-1}}\}$. For brevity, only part of the dataset is shown and discussed here.

F. CFD setup

The numerical models for the CFD and CAA have been calibrated and validated with the experimental data presented in this report. In the CFD approach, a compressible wall-resolved LES on a block-structured mesh is performed to simulate the spatially evolving turbulent boundary layer. The computational domain emulates the WAABLIEF test section, with the inlet plane at $x = -0.47\,\mathrm{m}$, which is in between the upstream measurement plane and the porous wall insert, to reduce the computational cost. The dimensions of the domain are $(x, y, z) = (0.65\,\mathrm{m}, 0.5\,h, 0.5\,\pi\delta_0)$, with $\delta_0 = 30\,\mathrm{mm}$.

To ensure comparability with the measurements, it is important to prescribe inflow conditions in the numerical simulation that match the characteristics of the boundary layer upstream of the porous insert in the WAABLIEF facility, as detailed in appendix A. This is accomplished by the turbulent inflow generation technique by Lund et al. [29], where the turbulent boundary layer profile at a downstream plane is rescaled to the target boundary layer momentum thickness and friction Reynolds number measured in the experiment and introduced at the inlet. To reduce acoustical reflections at the inlet, the fluctuations are injected by means of the vortical-flow characteristic boundary condition (VFCBC) [30]. The usual characteristic boundary conditions are applied at the outflow and upper boundaries of the domain. In the spanwise direction, periodic boundary conditions are applied. Additionally, a sponge layer at the upper and outflow boundaries is supposed to reduce spurious reflections and enforce a zero pressure gradient in the streamwise direction. The setup is sketched in Fig. 4.

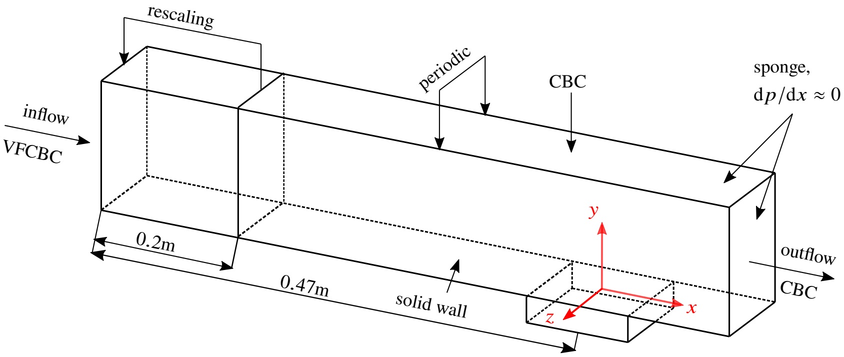

Fig. 4 Sketch of the computational domain and the boundary conditions applied.

The porous material is modeled by Eq. (1) as a medium with continuous properties, derived by means of the calibration setup mentioned in Section II.C. The metrics of the structured mesh used to resolve the three presented wall-insert configurations are summarized in Table 2. The details of an additional coarser mesh simulation are listed for the d_c = 4.5 mm case. The comparison between the two mesh-refinement levels of the d_c = 4.5 mm configuration serves as a basic mesh convergence analysis, which will be further assessed in future work.

Table 2 Metrics of the CFD simulation meshes. Provided are (i) the number of cells used to resolve the regions of both the main *channel* and the *porous medium* (ii) and the order of the cell dimensions in inner-scaled units. *Coarse* refers to a version of the simulation with fewer cells.

	Number of cells, -				
d_c, mm	*channel*	*porous medium*	x^+, -	y^+_{min}, -	z^+, -
0.0	120×10^6	-	15	<0.54	10
3.5	122×10^6	15×10^6	6-15	<0.87	8.5-17
4.5	122×10^6	15×10^6	6-15	<0.86	8.3-17
4.5 (coarse)	77×10^6	9×10^6	6-24	<0.95	8.7-19

For the definition of the time-step of the simulations, the Courant–Friedrichs–Lewy (CFL) number is provided:

$$\mathrm{CFL} = (U\Delta t)/\Delta x, \tag{7}$$

where Δx is the streamwise length of the mesh, U is the streamwise velocity through the mesh cell, e.g., the outer flow velocity, and Δt is the time-step of the solver. This quantity impacts the numerical stability of the simulation given the chosen solver. With the standard mesh, the CFL number of the porous wall-insert simulations lies around 0.745 and 0.796 for the solid-walled reference case. The *coarse* mesh for the d_c = 4.5 mm case achieves a CFL number around 0.497.

Consider the simulated boundary layer with both the standard and *coarse* mesh in Fig. 5a. The computed profiles for the mean-velocity profile, TI, and turbulent length scale agree well with the HWA data. The TI of the standard mesh more closely matches the data, especially above y/δ = 0.6, where the coarser mesh appears to deviate slightly from the measurements.

The difference in the high-frequency slope of the WPS in the *coarse*-meshed simulation and RMP data indicates a potential error in the modeling of the energy cascade in the simulation (see Fig. 5b). While the standard mesh shows a larger offset in the WPS to the data at high frequencies, the WPS slope in this region is correctly modeled. The WPS on the surface underneath the porous medium calculated with the standard mesh similarly match the measurement data more closely. Further comparison between the experimentally obtained data and the CFD predictions is presented in Section III.A.

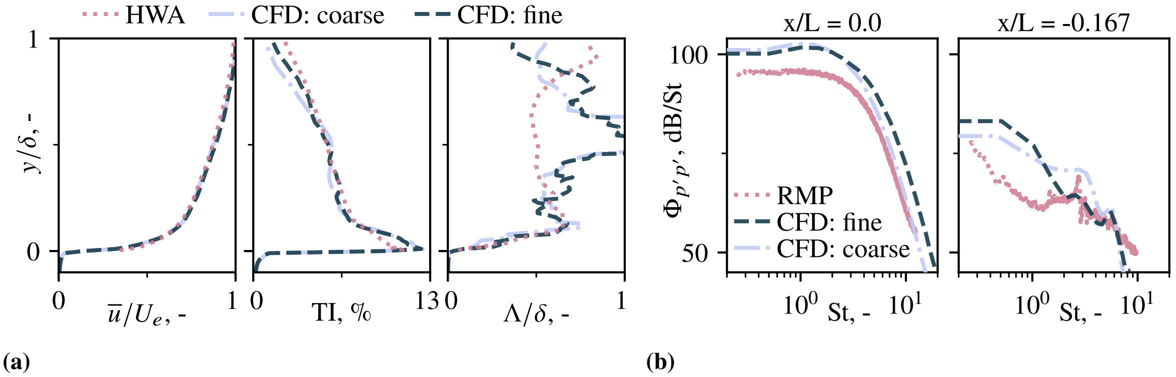

Fig. 5 Comparison between wind-tunnel measurements (HWA and WPS) and simulation data with the standard, i.e., ***fine*****, and the** ***coarse*** **mesh. The conditions are $d_c = 4.5\,\mathrm{mm}$ and $U_e = 15\,\mathrm{m\,s^{-1}}$. (a) Boundary-layer profiles for $x/L = 0$; (b) WPS on the upper ($x/L = 0$) and lower surface ($x/L = -0.167$) of the porous wall-insert.**

The permeability Reynolds number $\mathrm{Re}_K = u_\tau K^{1/2} \nu^{-1}$ is an important parameter for quantifying the wall-permeability effect on the boundary-layer flow and the flow within the porous medium [31]. Using the wall-shear velocity obtained through the simulations, Re_K averaged over both the spanwise direction and time (see Fig. 6) is provided along the streamwise extent of the material. The coarse-mesh simulation of the $d_c = 4.5\,\mathrm{mm}$ case does not achieve as high of a peak value near the start of the porous wall-insert as the standard mesh simulation.

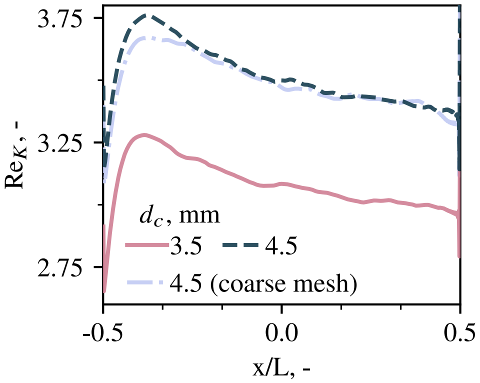

Fig. 6 Variation of the permeability Reynolds number over the streamwise extent of the porous wall-insert for different d_c and mesh-refinement levels.

III. Results

The purpose of this section is twofold. First, the experimental wind-tunnel data are used to validate the CFD simulations in Section III.A and discuss the impact of the porous materials on the turbulent boundary layer flow in Section III.B. Second, a brief description of the internal flow within the porous wall-inserts is given in Section III.C using the CFD data.

A. Validation of the CFD simulations

For the comparison between the experimental and simulation data, a single streamwise profile (x/L) of a single velocity case (U_e) is shown for each wall-insert (d_c) for brevity. The results of each configuration are shown to validate the correct modeling of the baseline and the porous materials, which partially depend on the calibration discussed in Section II.C.

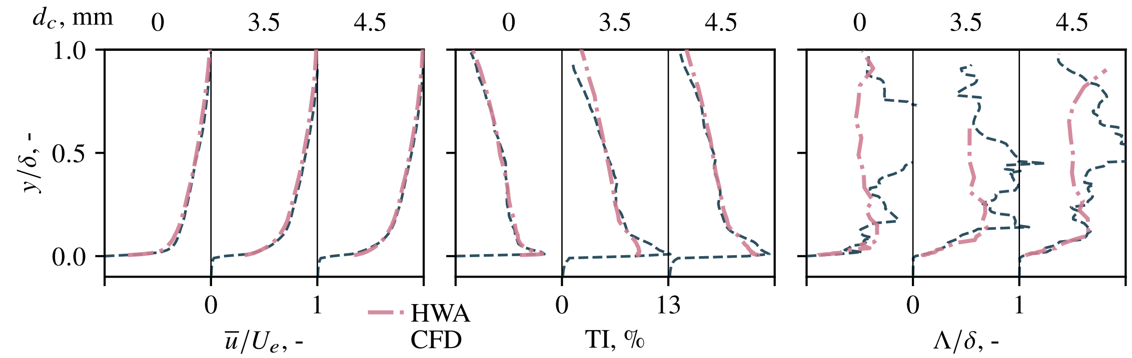

Fig. 7 Comparison between HWA and CFD data for the three wall-inserts. The conditions are $x/L = 0$ and $U_e = 15\,\mathrm{m\,s^{-1}}$. The profiles highlighted for each of the three wall-insert cases use the same x-axes limits, as indicated for the middle case of each quantity.

The boundary-layer profiles of several velocity-related quantities are compared in Fig. 7. The mean-flow velocity profile shows a close agreement, only differing slightly in the curvature near the wall. For the solid wall case, the CFD-derived velocity profile appears to have a larger shape factor than the HWA-derived profile.

The TI for the solid wall provides an equally excellent match between CFD and HWA. However, for the porous-walled cases, the CFD returns a slightly larger peak value of TI near the wall, i.e., $y/\delta < 0.2$, and a smaller value of TI near the upper half of the boundary layer, i.e., $y/\delta > 0.5$. Still, the TI is rather similar in magnitude and profile trend. For instance, the near-wall increase in TI starts near the same y/δ for both CFD and HWA data.

The turbulent length-scale profile does show a larger difference between both datasets. Here, the CFD data show several large peaks in Λ/δ at various y/δ, which are not present in any of the HWA data. It can only be speculated that, with a longer simulation period, the statistics of the turbulent flow might converge closer to the profiles acquired in the wind tunnel. Near the wall at $y/\delta < 0.25$, the small peak in Λ appears to be very similar to the experimental data. The porous material with $d_c = 4.5$ mm even exhibits a close match with the wind-tunnel turbulent length scale data.

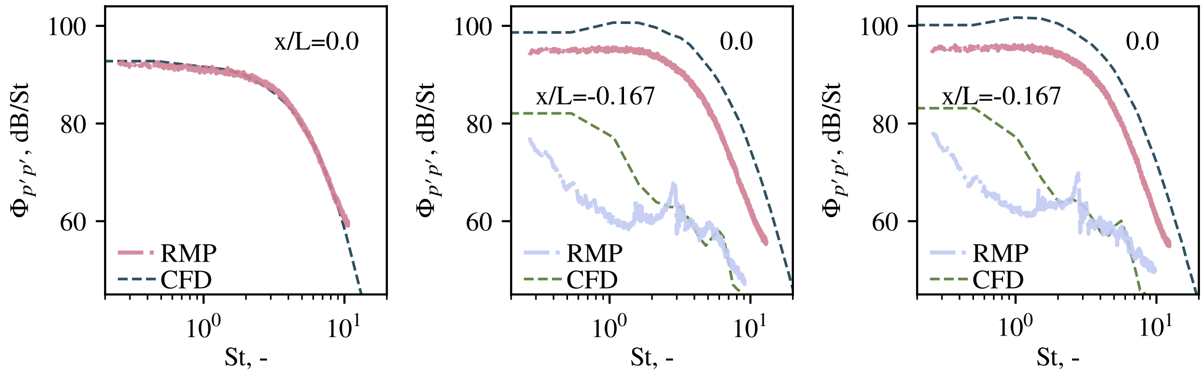

(a) **(b)** **(c)**

Fig. 8 Comparison between the WPS of RMP and CFD data for the three wall-inserts. The conditions are $U_e = 15\,\mathrm{m\,s^{-1}}$. Wall-inserts are: (a) Solid, $d_c = 0$ mm; (b) Porous with $d_c = 3.5$ mm; (c) Porous with $d_c = 4.5$ mm.

The WPS are another important metric to be validated if the CFD data is to be used for CAA in future investigations. For the porous materials, two streamwise probe points are shown, one on the upper surface of the material at $x/L = 0$, and one on the lower surface of the material at $x/L = -0.167$. The solid-walled case shows a perfect match between the simulation and experimental data (see Fig. 8a). On the contrary, the porous-walled cases are less clear-cut (see Figs. 8b and 8c). While the RMP data on the upper surface of the porous materials lack some energy with respect to the CFD data, the trend and, thus, the underlying cascade of turbulent structures appear similar. The origin of the difference in amplitude of both WPS cases remains unclear. For the lower surface of the porous wall-insert, the WPS match closely within $\mathrm{St} \in (3, 7)$. The WPS peaks within this range are likely due to resonance associated with either the insert height or a fraction of its length, e.g., the distance from the sampling point to the upstream or downstream solid wall of the wall-insert cavity. For Strouhal numbers above this threshold, the increased WPS compared to the CFD data might be an effect of the added turbulence linked to the porous-material skeleton, whereas the simulation models the medium as a continuum with volume-averaged properties. Similarly, at St below 3, the WPS feature lower values for the experiments compared to the simulations, possibly due to the larger turbulent scales being inhibited from reaching the lower porous-material surface by the porous structure. The lack of modeling of the porous-material skeleton is likely not the cause for the discrepancy in WPS for the upper surface, as surface roughness is linked to an increase in wall-pressure fluctuations [7, 9, 32].

The *flow-through* configuration of the porous-material calibration, i.e., with the flow perpendicular to the porous media interface, may not perfectly represent the porous wall-insert case considered in this validation study. The empirical parameters used to model the tangential momentum transfer at the fluid-porous interface [33, 34] are not considered in this case due to the lack of reference for them in the calibration data. Still, the considered CFD setup is generally capable of approaching the experimentally obtained data quite closely. This outcome indicates that the porous material calibration is correct and that the volume-averaged approach, while possibly impacting the overall CFD results, can constitute an acceptable simplification for modeling a grazing flow over a porous material. For the sake of completeness, the boundary-layer parameters derived from the CFD data at several streamwise positions are provided in appendix B.

B. Impact of porous materials on the boundary layer

For the HWA measurements, all streamwise solid-walled boundary layer profiles collapse well onto each other, indicating that there is no strong streamwise pressure gradient (see Fig. 9a). The TI gradually increases towards the wall, peaking around $y/\delta = 0.01$, after which the TI decreases again towards the wall.

In comparison, for the porous-walled cases, the boundary layer shows a strong dependence on the streamwise coordinate along the porous material, in both velocity and TI (see Fig. 9b). Considering the changes in the boundary-layer profiles while moving in the streamwise direction over the porous surface, there is a loss in flow velocity, a decrease in the shape factor, and an increase in TI below ca. $y/\delta < 0.3$. Moreover, with the increasing d_c, the velocity and TI at the wall increase (see Fig. 9c). Compared to the solid-walled case, both porous material cases feature a much shallower $\overline{u}/U_e$ profile. Conversely, increasing U_e has little impact on the shape of the non-dimensionalized velocity profile (see Fig. 9d). The TI near the wall ($y/\delta < 8 \times 10^{-2}$) decreases with the increasing U_e.

The change in the boundary layer also impacts the unsteady-pressure fluctuations at the wall. The WPS in the low-frequent range (St < 3) increase when going from the solid-walled case to either of the porous configurations (see Fig. 10a). Both porous materials exhibit a similar increase in WPS. With an increase in U_e, the WPS experience an increase over the entire frequency range (see Fig. 10b).

The dependence of the WPS on the streamwise coordinate over the porous material is observed in Fig. 10c. Going from $x/L = -0.33$ to $x/L = 0$, the low-frequent range (St < 3) of the WPS sees a decrease, whereas the high-frequency (St > 3) decay in energy remains similar. An overall decrease in the energy of the pressure fluctuations occurs. Going downstream, the WPS at low frequencies increase slightly. The starting frequency of the high-frequency decay in WPS shifts towards a higher frequency, but the slope of the WPS decay remains the same, resulting in an increase in WPS at high frequencies.

Both RMPs mounted on the lower surface of the porous media acquire an identical WPS, which differs in shape from the upper-surface WPS. These lower-surface WPS are likely mostly impacted by the propagation of pressure fluctuations, turbulent structures within the porous material, and resonance linked to the wall-insert cavity, as mentioned in Section III.A.

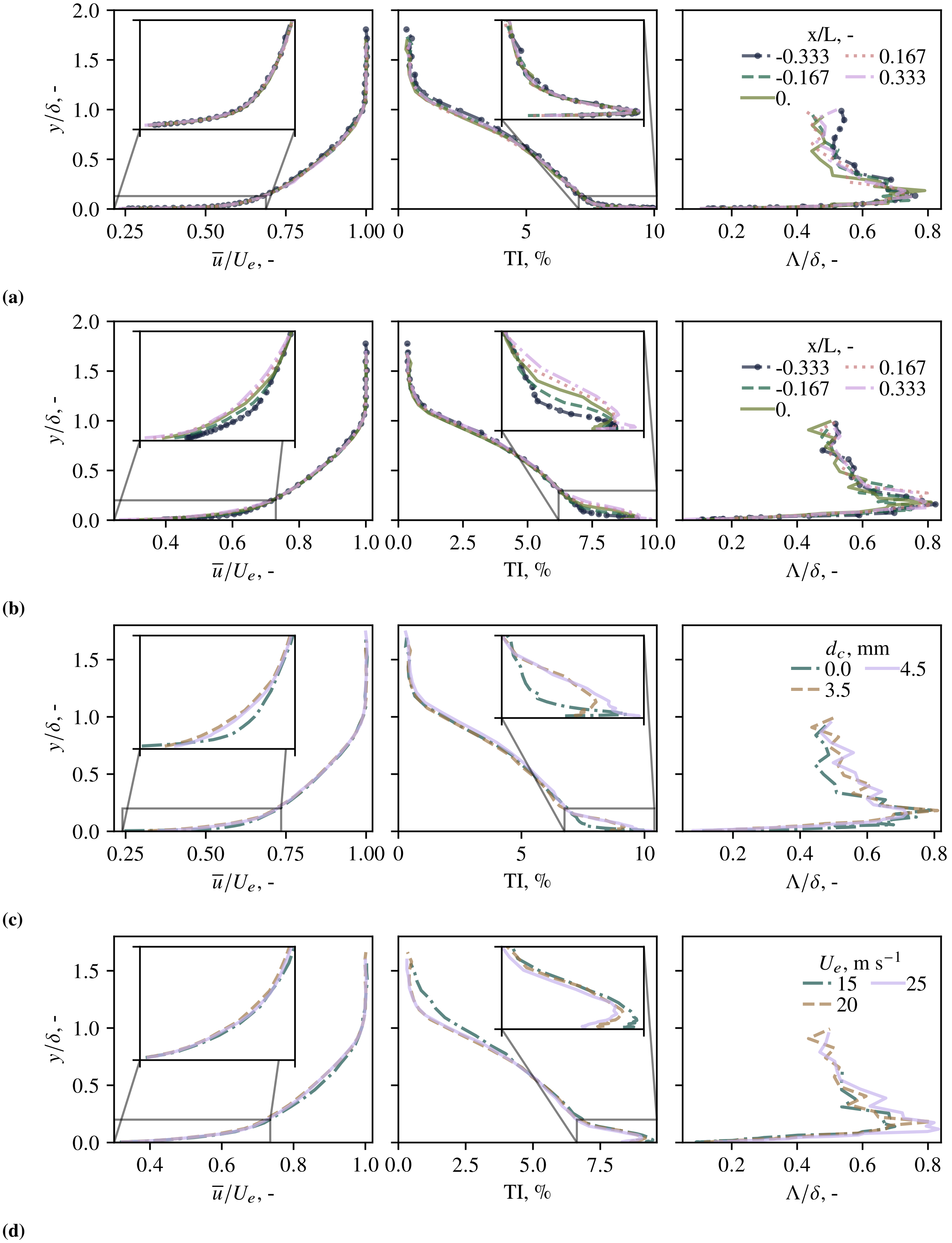

Fig. 9 HWA measurements. When not otherwise stated, the conditions are: $d_c = 3.5\,\mathrm{mm}$, $U_e = 20\,\mathrm{m\,s^{-1}}$, and $x/L = 0$. (a) Solid-walled case $d_c = 0\,\mathrm{mm}$; (b) Effect of x/L; (c) Effect of d_c; (d) Effect of U_e.

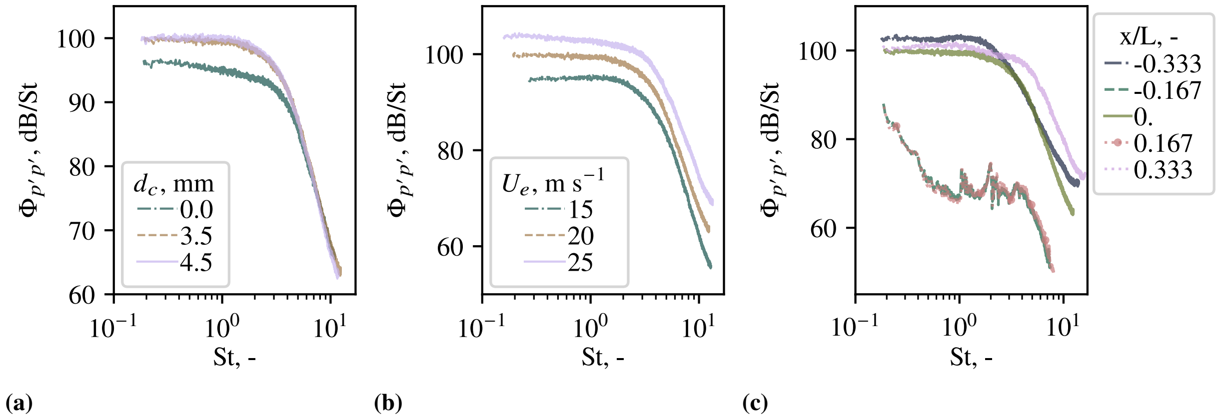

Fig. 10 WPS measurements. When not otherwise stated, the conditions are: $d_c = 3.5\,\mathrm{mm}$, $U_e = 20\,\mathrm{m\,s^{-1}}$**, and** $x/L = 0$**. (a) Effect of** d_c**; (b) Effect of** U_e**; (c) Effect of** x/L**.**

C. Porous-medium inner flow

With no velocity-related validation data within the material, the fluid structures within the porous medium cannot be validated. However, Breugem [31] shows that a volume-averaged simulation approach can achieve very usable results compared to a fully-resolved simulation using a similar wall-insert configuration, i.e., a porous channel wall with a structured porous skeleton. The above research mentions that the range of turbulent length scales in porous media is often very large: the smallest scales are of the order of the solid structure that forms the porous skeleton, and the largest ones are imposed by the external flow or the external geometry of the porous insert, i.e., as shown in Figs. 1b and 1c, respectively. Additionally, these scales tend to be well-separated, which benefits the volume-averaged modeling approach. As such, it is presumed that given the validation of the boundary layer over the porous wall-insert, the large-scale turbulent structures of the inner flow should be representative of the actual flow within the insert. Still, since the turbulence induced by the porous skeleton is not fully simulated, some flow structures inside the porous medium are not present in the CFD data. For instance, close to the surface, the skeleton directly defines where the flow can permeate the porous medium interface. Given the above, only the mean flow and its large vortical structures are discussed here. In this regard, the mean flow of both considered porous wall-inserts exhibits a very similar structure, as can be deduced from the streamlines in Fig. 11. This is due to the permeability Reynolds number [31, 35] being in the same regime of permeable-material flows (see Fig. 6).

The sudden transition from the solid wall to the porous insert results in shear flow over the porous surface. The flow enters the material at around $x/L = -0.4$, as shown in Fig. 11. Part of the internal flow forms a recirculation region at the leading edge of the porous wall-insert. Such a vortical structure possibly inhibits the flow from permeating the material toward the upstream part of the insert. This recirculation region additionally ejects flow from the material into the boundary layer at the leading edge of the insert, similar to the flow observed by Teruna [32] for their porous trailing edge. Likewise, this flow injection results in the local reduction of wall-shear stress, i.e., the decrease in $\mathrm{Re}_K \propto \sqrt{\tau_w}$, observed in Fig. 6. At the location of flow penetration into the porous insert, Re_K peaks.

At the downstream end of the porous wall-insert, another vortical structure is present, shown in more detail in Fig. 12. The boundary layer partly permeates into the upper layer of the porous material. The impingement of this relatively high-speed flow with the downstream edge of the cavity, in combination with the upward flow of air aiming to exit the material, results in this vortex. Ali et al. [9] have linked such vortical structures within porous media to additional noise over a small frequency band. The impingement of the boundary-layer flow with the downstream edge of the porous wall-insert cavity may additionally result in more drag. Comparing both porous wall-inserts, the lower permeability of the $d_c = 4.5\,\mathrm{mm}$ case results in somewhat higher velocity magnitudes compared to the $d_c = 3.5\,\mathrm{mm}$ one, especially in the downstream half of the porous medium (see Fig. 11). However, throughout most of the volume of the presented porous wall-inserts, the flow velocity is extremely low. Hence, only the uppermost part of these inserts aerodynamically contributes to the external flow.

In view of the above, a modeling approach for the flow within a porous material based on an electrical analogy may provide a more direct way of estimating the flow paths in the medium using the existing laws for computing the flow of current through electrical circuitry. Under this analogy, the local resistance of the material to flow would be linked to

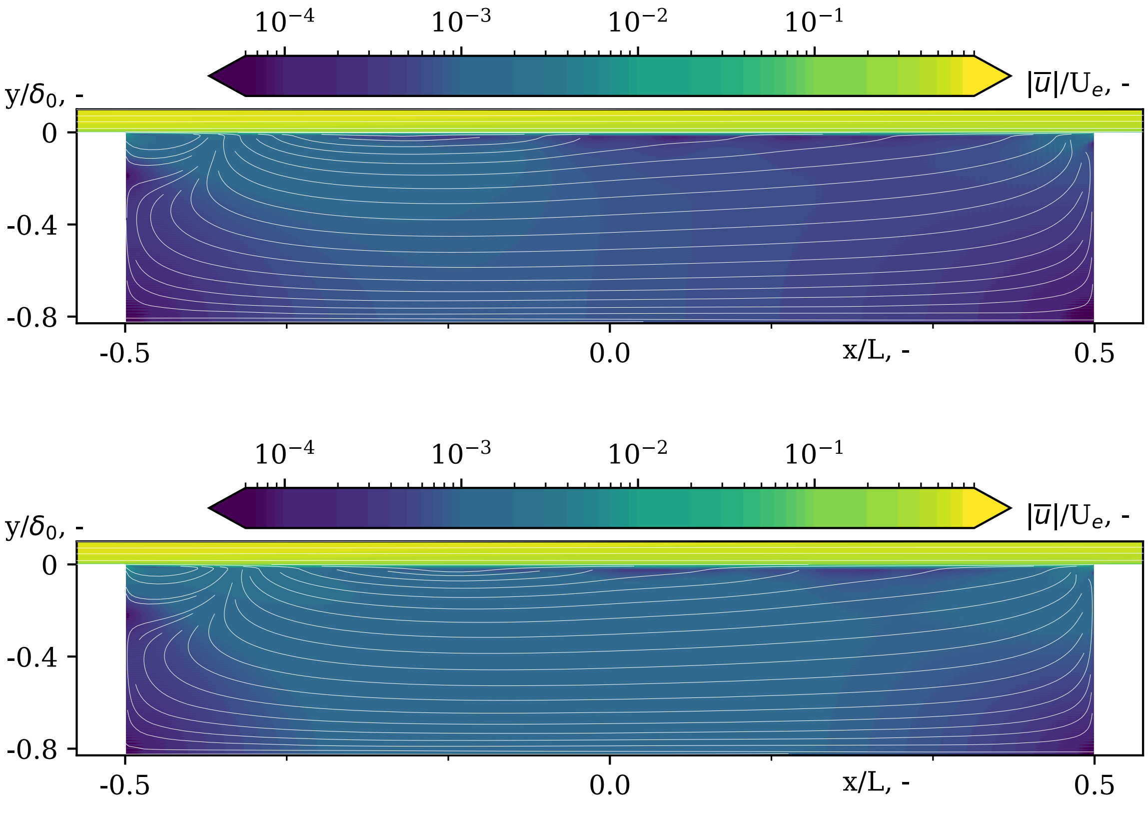

Fig. 11 Mean-flow magnitude within the porous wall-insert at $U_e = 15\,\mathrm{m\,s^{-1}}$. For the normalization of the y-coordinate, the constant $\delta_0 = 30\,\mathrm{mm}$ is used. Porous wall-insert cases: (a) $d_c = 3.5\,\mathrm{mm}$ and (b) $d_c = 4.5\,\mathrm{mm}$.

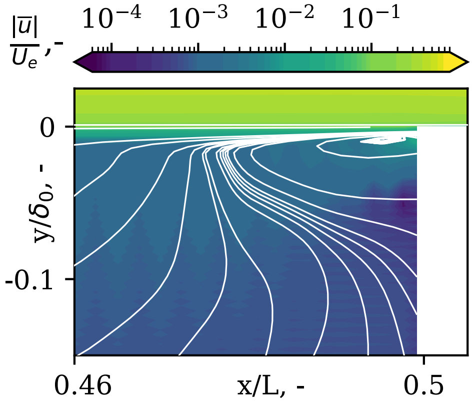

Fig. 12 Mean-flow magnitude of the vortical structure at the downstream edge of the porous wall-insert. The conditions are: $d_c = 3.5\,\mathrm{mm}$, $U_e = 15\,\mathrm{m\,s^{-1}}$, and $\delta_0 = 30\,\mathrm{mm}$.

the resistance of an electrical circuit element. Such a development would allow the porous medium to be tailored for the desired flow paths. For instance, the permeation of the boundary layer within the porous wall-insert may be more gradually controlled over its length, limiting the impingement on the trailing edge of the wall-insert and the formation of large vortices at either end of the porous medium, which has the potential to decrease both drag force and aerodynamic noise [9]. As mentioned in Section I, the publicly available benchmark dataset [12] developed in this research can serve as a test bench for this approach.

IV. Conclusion

Porous materials present a promising avenue for the abatement of aeroacoustic noise. Yet, to properly balance the attenuation of noise with the decrease in aerodynamic performance that can result from their use, the impact on the turbulent boundary layer needs to be better understood. In this regard, high-accuracy numerical simulations constitute an invaluable tool to investigate the physics involved in this interaction. Nevertheless, in order to accurately describe the internal flow field within the porous medium, these materials must be correctly modeled and validated through measurements.

The purpose of this research is two-fold: (i) developing a publicly available benchmark dataset of a boundary-layer flow over a porous wall-insert, and (ii) validating a new CFD simulation setup through the comparison of the numerical data against the HWA and RMP measurements of this dataset. Overall, the numerical results show a good agreement with the experimental data, for both the velocity-related quantities ($\overline{u}$ and TI) and the WPS. The results of the solid-walled test cases show no dependency on the streamwise coordinate within the test section. In comparison, both porous cases show a decrease in inertial energy in the streamwise direction along the porous material, shown by the more shallow boundary-layer profiles, and an accompanying increase in TI. With the increasing d_c, the $\overline{u}$ and TI increase at the wall. The same occurs with the increasing U_e, although with no change in the shape of the velocity profile.

The WPS of both solid and porous cases behave analogously to the boundary-layer profiles. The spectra for both porous-material cases exhibit a considerable increase in the low frequencies compared to the solid-wall case. Increasing flow velocity increases the WPS over the entire frequency range. The unsteady pressures feature a strong dependency on the streamwise position along the porous material. In particular, the low frequencies see a decrease in energy, whereas the high-frequencies exhibit an increase in energy when moving downstream along the medium. Furthermore, a thin film of high-velocity flow is present along the upper surface of the insert and drives vortices at the upstream and downstream edges of the cavity, which originate from the sudden local transitions between the solid wall and the porous material.

A more controlled permeation of the boundary layer into the porous medium may decrease drag and limit the formation or strength of the vortical structures, which have been shown to act as an additional noise source. Such control may be achieved by designing the flow paths that the flow-permeable material presents to flow permeating through it. A new modeling approach for porous media focused on determining these flow paths may lead to the development of novel, multi-layered porous materials suitable for different aeroacoustic applications. Such a modeling approach could be realized with an electric analogy for flow through porous media. The existing electric laws can then be exploited to find these flow paths, given the impedance of the porous media to achieve flow throughout the material.

A. Upstream boundary-layer characterization

For the purpose of replicating the results and using the data as a benchmark test case, several parameters of the boundary-layer velocity profile acquired with HWA are provided in Table 3. The shear velocity and derived friction coefficient are derived using the Clauser chart method [36]. The momentum-thickness Reynolds number is defined as:

$$\mathrm{Re}_\theta = (\theta U_e)/\nu. \tag{8}$$

Lastly, the mean velocity and TI profiles of the upstream HWA measurements are shown in Fig. 13.

Table 3 Boundary-layer parameters for the upstream HWA measurements ($x/L = -0.66$).

x/L, –	U_e, m s^{-1}	c_f, –	u_τ, m s^{-1}	δ, mm	δ^*, mm	θ, mm	H, –	Re_θ, –
−0.66	11.5	3.77×10^{-3}	2.96×10^{-1}	17.6	2.45	1.91	1.28	1438

B. CFD boundary layer profile characterization

The boundary-layer parameters derived from the CFD data at several streamwise profiles along the solid and porous wall-inserts are summarized in Tables 4 to 6. The defect thickness δ^* and momentum thickness θ only consider data above the porous medium interface, i.e., $y/\delta \geq 0$.

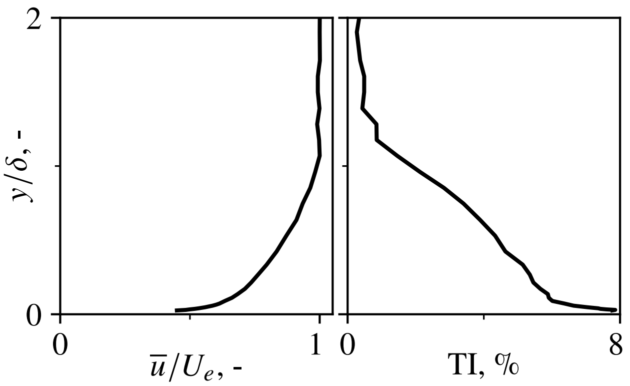

Fig. 13 Upstream HWA measurements ($x/L = -0.66$). The related boundary-layer parameters are provided in Table 3.

Table 4 CFD boundary-layer parameters for the simulation with $d_c = 0\,\mathrm{mm}$ and $U_e = 15\,\mathrm{m\,s^{-1}}$.

x/L, –	U_e, m s^{-1}	$c_{f,x}$, –	u_τ, m s^{-1}	δ, mm	δ^*, mm	θ, mm	H, –	Re$_\theta$, –
−0.333	14.9	3.22×10^{-3}	5.99×10^{-1}	26.5	4.37	3.18	1.37	3253
−0.167	14.9	3.16×10^{-3}	5.93×10^{-1}	26.6	4.37	3.18	1.37	3252
0.0	14.9	3.16×10^{-3}	5.93×10^{-1}	26.5	4.34	3.16	1.37	3231
0.167	14.9	3.20×10^{-3}	5.96×10^{-1}	26.5	4.34	3.16	1.37	3230
0.333	14.9	3.24×10^{-3}	6.00×10^{-1}	26.6	4.36	3.18	1.37	3242

Table 5 CFD boundary-layer parameters for the simulation with $d_c = 3.5\,\mathrm{mm}$ and $U_e = 15\,\mathrm{m\,s^{-1}}$.

x/L, –	U_e, m s^{-1}	$c_{f,x}$, –	u_τ, m s^{-1}	δ, mm	δ^*, mm	θ, mm	H, –	Re$_\theta$, –
−0.333	15.0	3.32×10^{-3}	6.11×10^{-1}	26.4	4.26	3.19	1.34	3275
−0.167	15.0	3.09×10^{-3}	5.90×10^{-1}	26.6	4.34	3.20	1.35	3293
0.0	15.0	2.99×10^{-3}	5.80×10^{-1}	26.6	4.43	3.22	1.37	3317
0.167	15.0	2.89×10^{-3}	5.71×10^{-1}	26.8	4.51	3.25	1.39	3344
0.333	15.0	2.84×10^{-3}	5.67×10^{-1}	26.8	4.58	3.28	1.40	3377

Table 6 CFD boundary-layer parameters for the simulation with $d_c = 4.5\,\mathrm{mm}$ and $U_e = 15\,\mathrm{m\,s^{-1}}$.

x/L, –	U_e, m s^{-1}	$c_{f,x}$, –	u_τ, m s^{-1}	δ, mm	δ^*, mm	θ, mm	H, –	Re$_\theta$, –
−0.333	15.0	2.92×10^{-3}	5.73×10^{-1}	26.5	4.30	3.19	1.35	3274
−0.167	15.0	2.70×10^{-3}	5.51×10^{-1}	26.6	4.36	3.18	1.37	3267
0.0	15.0	2.57×10^{-3}	5.38×10^{-1}	26.7	4.45	3.20	1.39	3289
0.167	15.0	2.48×10^{-3}	5.29×10^{-1}	26.8	4.58	3.25	1.41	3342
0.333	15.0	2.45×10^{-3}	5.26×10^{-1}	26.9	4.71	3.29	1.43	3392

Acknowledgments

The project received funding from the European Union's Horizon 2020 research and innovation programme within the project INVENTOR (innovative design of installed airframe components for aircraft noise reduction) listed under the grant agreement ID: 860538. Furthermore, the authors gratefully acknowledge the Gauss Centre for Supercomputing e.V. (`www.gauss-centre.eu`) for funding this project by providing computing time on the GCS Supercomputer HAWK at Höchstleistungsrechenzentrum Stuttgart (`www.hlrs.de`).

References

[1] Delfs, J., Faßmann, B., Lippitz, N., Lummer, M., Mößner, M., Müller, L., Rurkowska, K., and Uphoff, S., "SFB 880: aeroacoustic research for low noise take-off and landing," *CEAS Aeronautical Journal*, Vol. 5, No. 4, 2014, pp. 403–417. https://doi.org/10.1007/s13272-014-0115-2.

[2] European Parliament, Directorate-General for Internal Policies of the Union, Elliff, T., Cremasci, M. and Huck, V., *Impact of aircraft noise pollution on residents of large cities*, European Parliament, 2020. URL https://data.europa.eu/doi/10.2861/3570.

[3] Gallo, E., Zamponi, R., Zarri, A., Cansev, Y., and Schram, C., "Experimental Characterization of Flow Through Porous Fairings," 2023. https://doi.org/10.2514/6.2023-4175.

[4] Curle, N., "The influence of solid boundaries upon aerodynamic sound," *Proceedings of the Royal Society of London A*, Vol. 231, No. 1187, 1955, pp. 505–514. https://doi.org/10.1098/rspa.1955.0191.

[5] Amiet, R. K., "Noise due to turbulent flow past a trailing edge," *Journal of Sound and Vibration*, Vol. 47, No. 3, 1976, pp. 387–393. https://doi.org/10.1016/0022-460X(76)90948-2.

[6] Zamponi, R., Satcunanathan, S., Moreau, S., Meinke, M., Schröder, W., and Schram, C., "Effect of porosity on Curle's dipolar sources on an aerofoil in turbulent flow," *Journal of Sound and Vibration*, Vol. 542, 2023, p. 117353. https://doi.org/10.1016/j.jsv.2022.117353.

[7] Zamponi, R., "Investigation of turbulence-surface interaction noise mechanisms and their reduction using porous materials," Ph.D. thesis, Technische Universiteit Delft and von Karman Institute for Fluid Dynamics, Waterloosesteenweg 72, 1640 Sint-Genesius-Rode, April 2021. https://doi.org/10.4233/uuid:d332c7e3-87be-4ed6-aa71-e629ef77e07a.

[8] Rubio Carpio, A., Avallone, F., Ragni, D., Snellen, M., and van der Zwaag, S., "Mechanisms of broadband noise generation on metal foam edges," *Physics of Fluids*, Vol. 31, No. 10, 2019, p. 105110. https://doi.org/10.1063/1.5121248.

[9] Ali, S. A. S., Azarpeyvand, M., and da Silva, C. R. I., "Trailing-edge flow and noise control using porous treatments," *Journal of Fluid Mechanics*, Vol. 850, 2018, pp. 83–119. https://doi.org/10.1017/jfm.2018.430.

[10] Nelson, P., "Noise generated by flow over perforated surfaces," *Journal of Sound and Vibration*, Vol. 83, No. 1, 1982, pp. 11–26. https://doi.org/10.1016/S0022-460X(82)80072-2.

[11] Kisil, A., and Ayton, L. J., "Aerodynamic noise from rigid trailing edges with finite porous extensions," *Journal of Fluid Mechanics*, Vol. 836, 2018, p. 117–144. https://doi.org/10.1017/jfm.2017.782.

[12] Moriaux, O., and Zamponi, R., "A benchmark dataset for the grazing flow over porous materials," , Apr. 2024. https://doi.org/10.5281/zenodo.10955510.

[13] Van de Wyer, N., Zapata, A., Nogueira, D., and Schram, C., "Development of a test rig for the measurement of turbulent boundary layer wall pressure statistics," *2018 AIAA/CEAS Aeroacoustics Conference*, 2018. https://doi.org/10.2514/6.2018-3122.

[14] Ehlers, W., "Darcy, Forchheimer, Brinkman and Richards: classical hydromechanical equations and their significance in the light of the TPM," *Archive of Applied Mechanics*, Vol. 92, No. 2, 2022, pp. 619–639. https://doi.org/10.1007/s00419-020-01802-3.

[15] Office national d'études et de recherches aérospatiales, "INnoVative dEsign of iNstalled airframe componenTs for aircraft nOise Reduction," , May 2020. https://doi.org/10.3030/860538.

[16] Rubio Carpio, A., Merino Martínez, R., Avallone, F., Ragni, D., Snellen, M., and van der Zwaag, S., "Experimental characterization of the turbulent boundary layer over a porous trailing edge for noise abatement," *Journal of Sound and Vibration*, Vol. 443, 2019, pp. 537–558. https://doi.org/10.1016/j.jsv.2018.12.010.

[17] Derek B. Ingham, I. P., *Transport phenomena in porous media*, Pergamon, Oxford, 1998. https://doi.org/10.1016/B978-0-08-042843-7.X5000-4.

[18] Zamponi, R., Avallone, F., Ragni, D., Schram, C., and Van Der Zwaag, S., "Relevance of quadrupolar sound diffraction on flow-induced noise from porous-coated cylinders," *Journal of Sound and Vibration*, Vol. 583, 2024, p. 118430. https://doi.org/10.1016/j.jsv.2024.118430.

[19] Zamponi, R., Ragni, D., Van Der Zwaag, S., and Avallone, F., "Innovative coatings for reducing flow-induced cylinder noise by altering the sound diffraction," *Physics of Fluids*, Vol. 35, No. 12, 2023, p. 127120. https://doi.org/10.1063/5.0177263.

[20] Kanevče, G., and Oka, S., "Correcting hot-wire readings for influence of fluid temperature variations," *DISA Inf.*, Vol. 15, 1973, pp. 21–24. URL https://cir.nii.ac.jp/crid/1572543025369446528.

[21] Zamponi, R., Satcunanathan, S., Moreau, S., Ragni, D., Meinke, M., Schröder, W., and Schram, C., "On the role of turbulence distortion on leading-edge noise reduction by means of porosity," *Journal of Sound and Vibration*, Vol. 485, 2020, p. 115561. https://doi.org/10.1016/j.jsv.2020.115561.

[22] Moriaux, O. K., Zamponi, R., and Schram, C. F., "Semi-Empirical Calibration of Remote Microphone Probes Using Bayesian Inference," *Journal of Sound and Vibration*, 2023. https://doi.org/10.2139/ssrn.4526354.

[23] GRAS Sound & Vibration, "GRAS 40PH-10 Product Information," https://www.grasacoustics.com/products/special-microphone/array-microphones/product/ss_export/pdf2?product_id=830, Nov. 2023. Accessed on: 27/11/2023.

[24] Python Software Foundation, "Python Language Reference, version 3.9.12," , 2022. URL https://www.python.org.

[25] Moriaux, O., "Semi-Empirical Calibration using Bayesian inference (version 1.1)," , 2023. URL https://github.com/OMoriaux/SemiEmpiricalCalibrationBayesian.

[26] The MathWorks Inc., "Signal Processing Toolbox version: 8.7 (R2021b)," , 2021. URL https://www.mathworks.com.

[27] Whitmore, S. A., "Frequency response model for branched pneumatic sensing systems," *Journal of Aircraft*, Vol. 43, No. 6, 2006, pp. 1845–1853. https://doi.org/10.2514/1.20759.

[28] Moriaux, O., and Zamponi, R., "ASSIST: A Bayesian Post-Processing Tool for Remote Microphone Probe Calibration," , Feb. 2024. https://doi.org/10.2139/ssrn.4735018, (unpublished).

[29] Lund, T. S., Wu, X., and Squires, K. D., "Generation of turbulent inflow data for spatially-developing boundary layer simulations," *Journal of computational physics*, Vol. 140, No. 2, 1998, pp. 233–258. https://doi.org/10.1006/jcph.1998.5882.

[30] Guezennec, N., and Poinsot, T., "Acoustically nonreflecting and reflecting boundary conditions for vorticity injection in compressible solvers," *AIAA journal*, Vol. 47, No. 7, 2009, pp. 1709–1722. https://doi.org/10.2514/1.41749.

[31] Breugem, W.-P., "The influence of wall permeability on laminar and turbulent flows: Theory and simulations," Ph.D. thesis, Technische Universiteit Delft, Mekelweg 2, 2628 CD Delft, Jan. 2005. URL http://resolver.tudelft.nl/uuid:8f40233e-c326-4e60-8f18-09df59b88f47.

[32] Teruna, C., "Aerodynamic Noise Reduction with Porous Materials: Aeroacoustics Investigations and Applications," Ph.D. thesis, Technische Universiteit Delft, Kluyverweg 1, 2629 HS Delft, Mar. 2022. https://doi.org/10.4233/uuid:260cd874-c1ed-4155-bfdc-cf7fc3813ca6.

[33] Ochoa-Tapia, J. A., and Whitaker, S., "Momentum transfer at the boundary between a porous medium and a homogeneous fluid—I. Theoretical development," *International Journal of Heat and Mass Transfer*, Vol. 38, No. 14, 1995, pp. 2635–2646. https://doi.org/10.1016/0017-9310(94)00346-W.

[34] Mößner, M., and Radespiel, R., "Modelling of turbulent flow over porous media using a volume averaging approach and a Reynolds stress model," *Computers Fluids*, Vol. 108, 2015, pp. 25–42. https://doi.org/10.1016/j.compfluid.2014.11.024.

[35] Zamponi, R., Moreau, S., and Schram, C., "Rapid distortion theory of turbulent flow around a porous cylinder," *Journal of Fluid Mechanics*, Vol. 915, 2021, p. A27. https://doi.org/10.1017/jfm.2021.8.

[36] Clauser, F. H., "Turbulent boundary layers in adverse pressure gradients," *Journal of the Aeronautical Sciences*, Vol. 21, No. 2, 1954, pp. 91–108. https://doi.org/10.2514/8.2938.